



ELSEVIER

Contents lists available at ScienceDirect

## Pattern Recognition

journal homepage: [www.elsevier.com/locate/pr](http://www.elsevier.com/locate/pr)

## Structure-preserving smoothing of biomedical images

Debora Gil<sup>a,\*</sup>, Aura Hernández-Sabaté<sup>a</sup>, Mireia Brunat<sup>b</sup>, Steven Jansen<sup>c</sup>, Jordi Martínez-Vilalta<sup>d</sup><sup>a</sup> Computer Vision Center, Computer Science Department, UAB, Bellaterra, Spain<sup>b</sup> Instituto de Bioquímica Vegetal y Fotosíntesis, CSIC-Univ. Sevilla, Sevilla, Spain<sup>c</sup> Institute of Systematic Botany and Ecology, Ulm University, Germany<sup>d</sup> CREAF/Ecology Unit, UAB, Bellaterra, Spain

## ARTICLE INFO

## Keywords:

Non-linear smoothing  
 Differential geometry  
 Anatomical structures segmentation  
 Cardiac magnetic resonance  
 Computerized tomography

## ABSTRACT

Smoothing of biomedical images should preserve gray-level transitions between adjacent tissues, while restoring contours consistent with anatomical structures. Anisotropic diffusion operators are based on image appearance discontinuities (either local or contextual) and might fail at weak inter-tissue transitions. Meanwhile, the output of block-wise and morphological operations is prone to present a block structure due to the shape and size of the considered pixel neighborhood.

In this contribution, we use differential geometry concepts to define a diffusion operator that restricts to image consistent level-sets. In this manner, the final state is a non-uniform intensity image presenting homogeneous inter-tissue transitions along anatomical structures, while smoothing intra-structure texture. Experiments on different types of medical images (magnetic resonance, computerized tomography) illustrate its benefit on a further process (such as segmentation) of images.

© 2010 Elsevier Ltd. All rights reserved.

## 1. Introduction

Medical imaging scanners have been improving the quality of images over the years. Given that scanners capture either physical or chemical properties of tissue, the appearance of anatomical structures in images should be uniform. However, the presence of radiological noise (among other artifacts) disturbs structures homogeneity. It follows that images should be smoothed before any segmentation of anatomical structures. Medical imaging smoothing should homogenize the intensity inside anatomical structures, while preserving intensity changes at their boundaries without altering their shape. Existing smoothing methods for preserving image features (edges and corners) might be grouped into block-wise and differential operators.

Block-wise operators (like median, morphological [1], mean shift [2], or Kuwahara inspired [3]) replace the pixel intensity by a function (usually statistical [2,3]) of neighboring values. Since they can be related to image level-sets evolution (rather than image intensity evolution) they naturally preserve contrast changes. The counterpart is that evolution of image contours alters their shape. Contours in filtered images deform according to the shape of the structure element defining the pixel neighborhood. In many cases [1,3], even the smoothed image might present a block-wise appearance congruent with the shape of such structure element.

Differential operators use parabolic partial differential equations (PDE) to (iteratively) smooth an initial image [1]. Although higher order methods exist [4], many methods are given by second order elliptic operators admitting a formulation in general divergence form. Such methods have a physical interpretation in terms of heat diffusion and are backed by a solid mathematical theory [5].

For divergence-based methods, the redistribution of image intensity along time (iterations), as well as, final states are determined by the diffusion tensor. A main property is that evolution converges to a constant image unless the tensor cancels on some curves [5]. This is exploited by edge enhancement diffusions [6], which diffuse backwards (i.e. the tensor becomes negative) at pixels with an image gradient above a given threshold and like a standard heat equation otherwise. In this manner, they sharpen image contrast at edges while performing like a Gaussian filter at areas where contrast change is not significant. Although widely used by the medical imaging community, the choice of the threshold is a delicate issue [7–9] for preventing enhancement of noise and image artifacts.

In order to ensure smooth images, anisotropic diffusions [1] design positive tensors slowing down diffusion across structures and features of interest. Such features are determined by measures of image appearance discontinuity. Common trends are either the norm of image derivatives (first order for edges [10] and second order for ridges [11]) or global contextual discontinuities [12]. In order to ensure stability of the diffusion process, heat diffuses on the whole image plane, which implies convergence to a uniform intensity image [5]. This fact forces relying on a given number of

\* Corresponding author.

E-mail address: [debora@cvc.uab.es](mailto:debora@cvc.uab.es) (D. Gil).

iterations (termination problem) or adding close-to-data constraints to ensure preservation of the image most relevant features.

Close-to-data diffusions [13,14] add a zero order fidelity term quantifying the difference between the original and the (current) diffused image to the anisotropic formulation. The iterative scheme is the minimization of a (total variation) functional searching for a compromise between smoothing and similarity to original data. The weight that controls the tradeoff between the regularity and fidelity terms is related to the degree of filtering of the solution of the minimization problem. A main concern is that smaller details, such as texture and some structures are destroyed if such parameter is too small [4,15].

Finally, trace-based methods [16] remove first order terms from the divergence equation to make solutions consistent with the image level-sets geometry described by the diffusion tensor. Solutions are related to line integral convolution [17] along the diffusion tensor eigen-directions. Although sharp edges and curved structures are better preserved along the diffusion process, in the general case, a number of iterations must still be given in order to prevent convergence to constant final states. Besides, since the numeric scheme bases online integration of single vector fields [18] it cannot be easily generalized to diffusion on surfaces in volumetric data.

In this paper we introduce a differential operator, the structure-preserving diffusion, SPD, which restricts diffusion to a smooth approximation of image contours. Differential geometry arguments [19] ensure stability of the diffusion process. A main contribution is that SPD homogenizes gray-level along regular image contours without altering their shape. In this manner, SPD converges (i.e. the iterative scheme stabilizes) towards a non-uniform image presenting a uniform gray-level inside anatomical structures, while preserving transitions across tissue layers.

The contents of this paper are structured as follows. Our SPD approach is detailed in Section 2 and its mathematical issues are included in Appendix A. Validating experiments comparing with existing works are reported in Section 3 and an application illustrating SPD benefits is given in Section 4. Finally, concluding remarks are exposed in Section 5.

## 2. Implicit restricted diffusions

Smoothing methods provide a set of smoothed versions of a given (2D or 3D) function  $u_0(x_1, \dots, x_n) = u_0(x)$ . For PDE-based methods, the set of smoothed versions is a time (scale) dependant family,  $u(x, t)$ , that solves a PDE of parabolic type with initial condition  $u_0(x)$ . Many approaches for image smoothing are given by second order elliptic operators given in pure divergence form  $u_t = \text{div}(J \nabla u)$  with  $u(x, 0) = u_0(x)$  (1)

for  $\nabla u = (u_{x_1}, \dots, u_{x_n})$  the function gradient and  $u_t$  the derivative with respect to time. The symbol  $\text{div}$  is the divergence operator,  $J$  an  $n$ -dimensional symmetric (semi) positive defined tensor and  $F_1, F_0$  continuous functions defining first and zero order terms, respectively.

The behavior of solutions is univocally determined by the second order term given by the divergence defined by the diffusion tensor,  $J$ . The diffusion tensor, considered as linear map, diagonalizes in an orthonormal basis:

$$J = Q \Lambda Q^t = \begin{pmatrix} \xi_1^1 & \dots & \xi_1^n \\ \vdots & & \vdots \\ \xi_n^1 & \dots & \xi_n^n \end{pmatrix} \begin{pmatrix} \lambda^1 & \dots & 0 \\ \vdots & & \vdots \\ 0 & \dots & \lambda^n \end{pmatrix} \begin{pmatrix} \xi_1^1 & \dots & \xi_1^n \\ \vdots & & \vdots \\ \xi_n^1 & \dots & \xi_n^n \end{pmatrix} \quad (2)$$

for  $\lambda^1 \geq \dots \geq \lambda^n \geq 0$  the matrix of eigenvalues and  $\xi^i = (\xi_1^i, \dots, \xi_n^i)$  the corresponding (orthonormal) eigenvectors. A unique smooth solution exists as far as  $\lambda^i$  do not vanish ( $J$  strictly positive). Such

solution might be interpreted as redistributing (diffusing) the gray-values of the original image. Although this is convenient for image smoothing, the counterpart is that steady states (asymptotic behavior as  $t \rightarrow \infty$ ) are constant images [5]. This implies that the diffusion stopping time (iterations in numeric implementations) is a critical issue for restoring an image preserving meaningful structures [12]. The eigenvectors and eigenvalues locally describe the way mass distributes: an amount  $\lambda^i$  of mass travels along the direction given by  $\xi^i$ . In this context, diffusions split into isotropic (equal eigenvalues) and anisotropic (distinct strictly positive eigenvalues).

In [19], it is shown that the eigenvalue matrix  $\Lambda$  admits null eigenvalues as far as the associated eigenvectors define a differential manifold. Let  $\mathcal{D} = \langle \xi_1, \dots, \xi_k \rangle$  denote the eigenvectors of positive eigenvalues ( $\lambda^i = 1, i = 1, \dots, k$ ). If such vector space represents the tangent space to a manifold of  $\mathbb{R}^n$  (called integral variety of  $\mathcal{D}$  and noted from now on by  $M$ ), then the metric  $J$  is the projection onto  $M$  tangent space. Consequently a diffusion process governed by  $J$  would not take place in the whole space  $\mathbb{R}^n$  but just on the integral manifolds of  $\mathcal{D}$ . We will call it restricted diffusion.

The integrability condition ensuring that  $\mathcal{D}$  defines integral manifolds is a standard result on differential geometry known as the Frobenius Theorem [20]. This condition is always satisfied in the case that  $\mathcal{D}$  is a single vector field (so that integral manifolds are curves) or the perpendicular space to a single vector field (so that integral manifolds are  $n-1$ -dimensional spaces).

Although the restricted diffusion does not coincide with the heat equation for manifolds, it is an elliptic operator on the integral manifolds of  $\mathcal{D}$  (see Appendix and [19]). This guarantees existence and uniqueness of solutions in  $\mathbb{R}^n$  [19], which, restricted to  $M$ , have equal properties and asymptotic behavior as solutions to the heat equation [21]. Since the effect of the restricted diffusion operator may be regarded as diffusing on each of the integral manifolds separately, solutions converge towards a collection of manifolds (those given by  $\mathcal{D}$ ) of uniform gray-level [19]. This ensures that any numeric (iterative) scheme stabilizes at a non-uniform intensity function. Level-manifolds of the steady state approximate the original image contours, provided that  $\mathcal{D}$  represents their tangent space.

An interesting issue is that our restricted diffusion is an implicit formulation of a heat equation for manifolds. From a computational point of view, this endows several advantages over explicit formulations of the heat equation for manifolds. Explicit formulations might require computing a parametrization of the manifold. Although, in the case of curves, numeric schemes for ordinary differential equations (like Runge-Kutta [18]) can be used, for higher dimensions manifold integration is not straightforward. Our implicit formulation in  $\mathbb{R}^n$  coordinates might be solved, regardless of the dimension, using explicit Euler schemes for non-linear heat equations.

### 2.1. Structure-preserving diffusion

In the case of images,  $I(x, y)$ , the second moment matrix or structure tensor provides a good description of their local structures. The structure tensor matrix describes the gradient distribution in a local neighborhood of each pixel by averaging the projection matrices onto the image gradient:

$$ST(\rho, \sigma) = g_\rho * \left[ \begin{pmatrix} I_x(\sigma) \\ I_y(\sigma) \end{pmatrix} (I_x(\sigma), I_y(\sigma)) \right] = \begin{pmatrix} g_\rho * I_x^2(\sigma) & g_\rho * I_x(\sigma) I_y(\sigma) \\ g_\rho * I_x(\sigma) I_y(\sigma) & g_\rho * I_y^2(\sigma) \end{pmatrix}$$

Image derivatives are computed using Gaussian kernels,  $g_\sigma$ , of variance  $\sigma$  (differentiation scale):

$$I_x(\sigma) = g(\sigma)_{x'} * I \quad \text{and} \quad I_y(\sigma) = g(\sigma)_{y'} * I$$

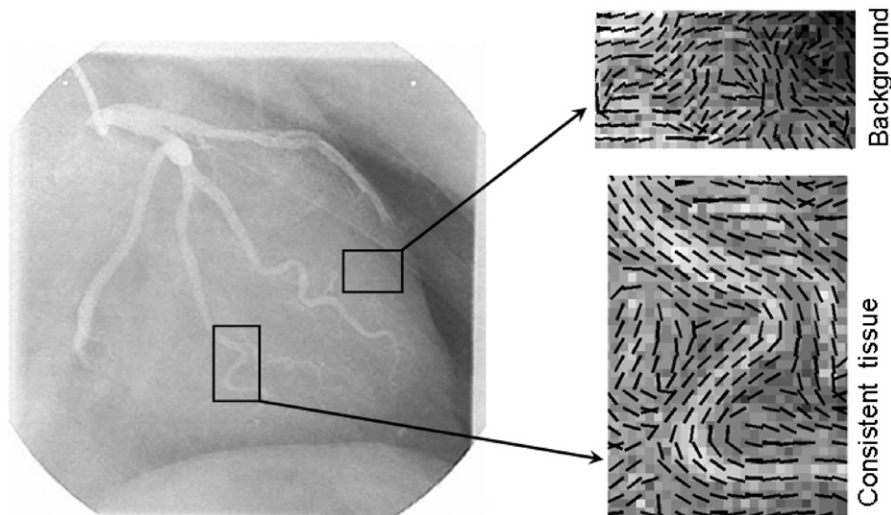


Fig. 1. Vector field representing level curves of an angiography for a vessel (bottom-right image) and a background structure-less area (upper-right image).

The projection matrix onto  $(I_x(\sigma), I_y(\sigma))$  is averaged using a Gaussian of variance  $\rho$  (integration scale). Since  $ST(\rho, \sigma)$  is the solution to the heat equation with initial condition the projection matrix, its eigenvectors are differentiable (smooth) vector fields that represent image level-sets normal (principal eigenvector,  $\xi$ ) and tangent (secondary eigenvector,  $\xi^\perp$ ) spaces. In the absence of corners (like anatomical contours in bottom right image in Fig. 1), the vector  $\xi^\perp$  is oriented along image consistent contours (in the sense of regular differentiable curves [20]). At textured or noisy regions,  $\xi^\perp$  is randomly distributed (upper right image in Fig. 1) and defines self-intersecting curves with a large number of corners. At such singular points (self-intersections and corners) the tangent space expands the whole plane (i.e. covers more than one direction).

Our structure-preserving diffusion is given by

$$I_t = \text{div}(Q A Q^t \nabla I), \quad I(x, y, 0) = I_0(x, y) \quad (3)$$

with

$$Q = (\xi^\perp, \xi) \quad \text{and} \quad A = \begin{pmatrix} 1 & 0 \\ 0 & 0 \end{pmatrix}$$

for  $\xi$  the principal eigenvector of  $ST(\rho, \sigma)$ .

Given that  $\xi^\perp$  spatial distribution is a well-defined 1D vectors field oriented along regular structures (bottom right image in Fig. 1), SPD smoothes image gray values along them. Meanwhile, at textured and noisy regions,  $\xi^\perp$  expands the whole plane (upper right image in Fig. 1) and, thus, SPD performs like a Gaussian filter, in the sense that solutions converge to a constant value. Therefore solutions to (3) converge to a non-trivial image that preserves the original image main features as curves of uniform gray-level [19]. In this manner, SPD output achieves a uniform response to local image descriptors suitable for a further detection and segmentation of image (anatomical) regions.

### 3. Experiments

The goal of our experiments is to show the improvement in quality of SPD images (compared to other filtering approaches) for a further identification of anatomical structures. In order to illustrate SPD benefits regardless of the image modality and anatomic geometry considered, two different data sets have been considered:

- Cardiac magnetic resonance (MR) images. Images have been extracted from a data set of healthy volunteers provided by Creu Blanca Clinic. Images have been acquired using a Siemens Avanto

1.5T (Erlangen, Germany) with a spatial resolution from  $1.3 \times 1.3$  to  $1.7 \times 1.7$  mm/pixel. The selected images consists of 12 images in short axis (SA) views and 8 in long axis (LA) views.

- Liver computerized tomography (CT) volumes. Images have been selected from the public database (sliver07.isi.uu.nl) collected for sliver07 competition hosted at MICCAI07 [22]. CT images were acquired with scanners from different manufacturers (4, 16 and 64 detector rows) with a pixel spacing between 0.55 and 0.80 mm and the inter-slice distance from 1 to 3 mm. We have considered 125 images in transversal view uniformly sampled on five CT-volumes (25 images per volume).

Target structures (myocardium for MR and liver for CT) have been identified by k-means unsupervised clustering on the intensity of the original and smoothed images. Following the literature [22], the quality of segmentations has been assessed by comparing them to manual segmentations in terms of region overlap and distance to manually traced contours. In particular, if we denote by  $X$  the reference segmentation and  $Y$  the automatic one, we have considered the following scores:

1. *Volumetric overlap error (Jaccard measure [23])*. It is given in terms of the percentage in region overlap between two segmentations,  $X$  and  $Y$ :

$$VOE := 100(1 - |X \cap Y| / |X \cup Y|)$$

for  $|\cdot|$  the number of pixels in a given region.

2. *Average symmetric surface distance*. The distance of an arbitrary voxel,  $y$ , to a volume  $X$  is defined as:  $d_X(y) = \min_{x \in X} \|y - x\|$ , for  $\|\cdot\|$  the Euclidean norm. The average symmetric surface distance is defined as the average between  $d_X(y)$  and  $d_Y(x)$  as

$$AvSSD = \frac{1}{|X| + |Y|} \left( \sum_{x \in X} d_Y(x) + \sum_{y \in Y} d_X(y) \right)$$

3. *Maximum symmetric surface distance*. It is given by the maximum of  $d_X(y)$  and  $d_Y(x)$ :

$$MxSSD = \max_{x \in X} (\max_{y \in Y} (d_Y(x)), \max_{y \in Y} (d_X(y)))$$

All scores are given in pixels and give 0 for a perfect segmentation.

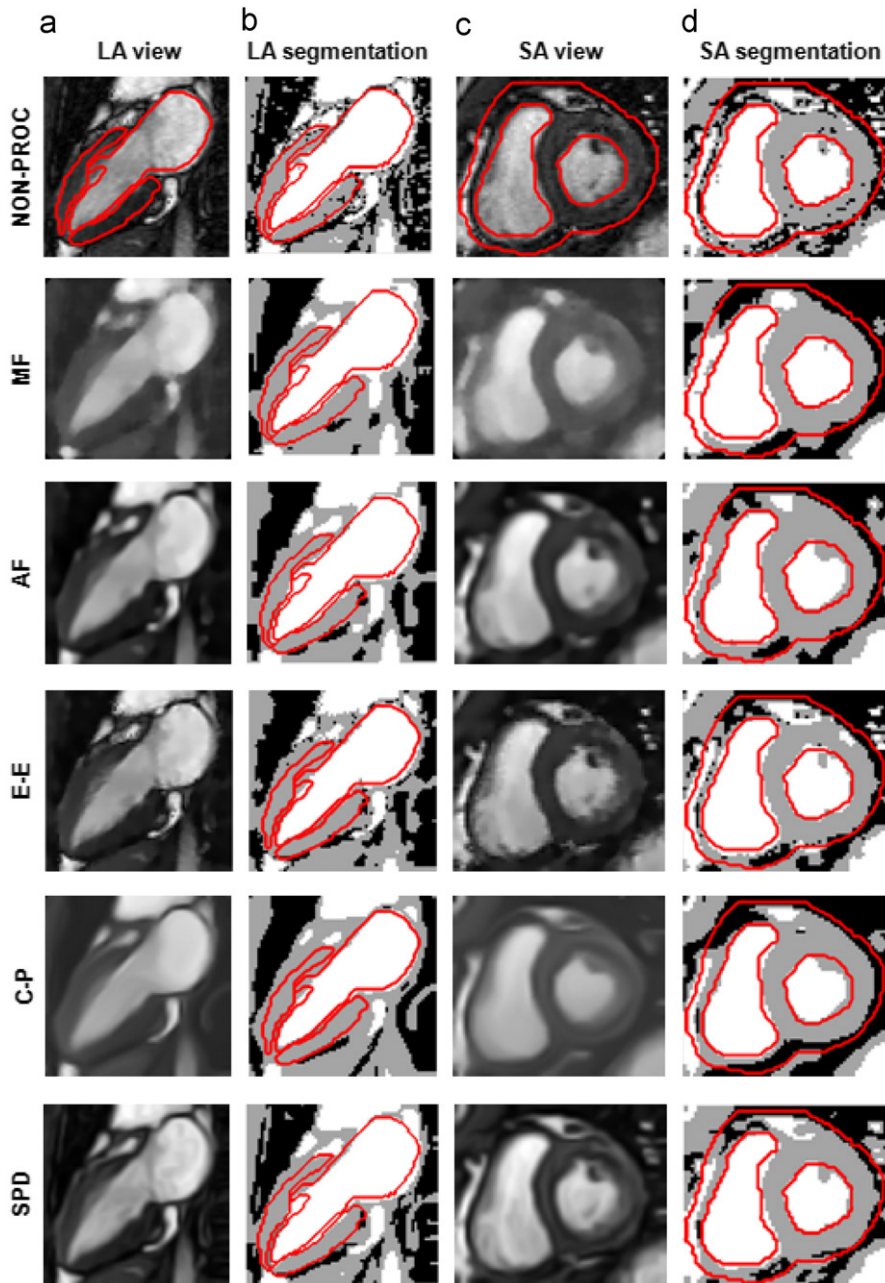


Fig. 2. Performance of smoothing approaches on cardiac MRI.

We have compared SPD to four representative techniques: edge-enhancement (labeled E-E), anisotropic diffusion (labeled AD), curvature-preserving (labeled C-P) and median filtering (labeled MF). Edge-enhancing, anisotropic diffusion and SPD were computed using an explicit (finite difference) iterative scheme. Edge-enhancing and anisotropic diffusion were stopped after 20 iterations, while SPD images are the steady states obtained by stabilization of the numeric scheme [24]. Curvature-preserving images have been computed using default parameters,<sup>1</sup> except for the anisotropy rate, which was set to 1. We recall that such pure anisotropic case should asymptotically behave like SPD and converge to a collection of curves of constant intensity. In order to check the latter assumption and for the sake of a faithful comparison to the other PDE-based methods, 20 iterations were

considered. Finally, the size of the window for the median filter was chosen depending on the resolution of the images of each data set and was set to  $3 \times 3$  for cardiac MR and  $5 \times 5$  for liver CT images.

### 3.1. Results for cardiac MR

Manual segmentations were defined as both ventricles (left ventricle, LV, and right ventricle, RV) excluding trabeculae and papillary muscles. We observe that this introduces a base-line systematic error in *MxSC*, especially for segmentation of myocardial walls in SA views (due to the trabeculae).

Representative SA and LA cuts and their region segmentation for non-processed and filtered images are shown in Fig. 2. Three regions have been segmented: blood (shown in white), myocardial walls (shown in gray) and background (shown in black).

<sup>1</sup> Software available at [www.greyc.ensicaen.fr/dtschump/greycstorage/](http://www.greyc.ensicaen.fr/dtschump/greycstorage/).

Manual contours are plotted in red on segmented images and also on the non-processed ones for a better discrimination of cardiac walls. Images in LA cuts (Fig. 2(a)) mainly show the LV as a parabolic 'U'-shaped structure. There are two areas difficult to segment. First, the thin background layer separating the LV and the bottom adjacent tissue should be preserved. Second, the piece of the RV appearing on the right bottom part of images as a small bright structure should not merge to the LV. The heart in SA cuts (Fig. 2(c)) clearly shows both ventricles and the LV presents a circular geometry. In this case, there are three small structures that should be preserved for an accurate segmentation. First, the RV wall (thin dark layer on the left side of images), in order to avoid merging blood pool with adjacent tissue. Second, the weak separation between heart and bottom adjacent tissue and, finally, the sharp geometry of trabeculae muscles (the small structures appearing at the first quadrant of the LV endocardium) in order to discard them from LV shape models. Table 1 reports the statistical ranges of the quality scores for blood and myocardial wall in LA and SA views and a total range for all views and regions. The results have been split into blocks corresponding to each method. Bold face is used to highlight the best ranges.

In non-processed images, blood is accurately identified (presenting a high accuracy rate in Table 1) in both views and myocardial tissue is separated from adjacent structures. Small structures (such as RV thin wall and trabeculae muscles in Fig. 2(d)) are partially missing and myocardial regions are corrupted by spurious pixels wrongly classified as background. Although this does not significantly affect SA wall detection rate it

substantially rises segmentation error for LA views. Since, for both views, spurious pixels wrongly classified in original views are removed in all filtered images, blood detection rates are similar for all methods. However, the geometry of the segmented anatomical structures varies across smoothing methods. Compared to PDE-based methods, MF is more aggressive to shape geometry and is prone to merge adjacent tissue (RV and bottom tissue in Fig. 2(b)) and lose thin and small structures (RV wall and trabeculae in Fig. 2(d)). Systematic tissue merging increases the average distance for LA wall, while structure lost affects maximum distances in SA blood and wall segmentations (Table 1, 2nd block). AF images present a general decrease in intensity sharpness (Fig. 2(a), (c)), which equally affects segmentation accuracy (Table 1, 3rd block) for SA and LA walls. In qualitative terms (Fig. 2(d)), sharpness decrease might merge myocardium with surrounding tissue and oversmooth structure shape (like trabeculae). We observe that C-P (Table 1, 4th block) quickly degrades intensity sharpness at small structures which distorts its shape (like trabeculae in Fig. 2(d) and RV in Fig. 2(b)). This might be attributed to numerical errors inherent to the Runge-Kutta scheme used in its implementation, which prevent convergence to the theoretical collection of curves of constant gray-level. We would like to note that for a small number of iterations (at most 2 as suggested in [16]) it behaves like AF. Those images filtered with E-E present a good preservation of intensity sharpness at the cost of a pixelized texture appearance (Fig. 2(a), (c)). It follows that segmentations keep separations between myocardium and adjacent tissue but restore discontinuous (RV wall in Fig. 2(d)) and irregular profiles. Although in overall terms, E-E is the second best performer (Table 1, 5th block), texture enhancement might drop its performance at images prone to present noisy backgrounds (LA wall). Finally, SPD is the best performer with top ranges for eight specific scores and optimal total ranges for the three quality measures. Images in Fig. 2 show that the steady states achieved by SPD present a good compromise between noise removal and restoration of continuous anatomical structures.

**Table 1**  
Quality scores ranges for cardiac MRI.

	AvSD	MxSC	VOE
<b>Non-proc</b>			
LA Blood	1.63 ± 1.05	6.66 ± 3.53	27.94 ± 15.95
LA Wall	3.28 ± 3.37	13.85 ± 7.81	77.05 ± 30.51
SA Blood	1.01 ± 0.88	6.38 ± 4.70	29.24 ± 19.73
SA Wall	1.34 ± 1.06	<b>7.15 ± 3.85</b>	49.85 ± 25.27
Total	1.81 ± 1.01	8.51 ± 3.57	46.02 ± 22.99
<b>MF</b>			
LA Blood	1.30 ± 0.58	6.49 ± 3.04	20.08 ± 11.13
LA Wall	2.27 ± 1.69	13.66 ± 8.38	<b>47.92 ± 24.72</b>
SA Blood	1.33 ± 0.83	8.33 ± 4.10	33.38 ± 14.54
SA Wall	1.63 ± 1.20	10.69 ± 7.48	49.26 ± 24.14
Total	1.63 ± 0.45	9.79 ± 3.10	37.66 ± 13.75
<b>AF</b>			
LA Blood	1.14 ± 0.63	6.92 ± 3.58	18.73 ± 12.08
LA Wall	1.86 ± 1.05	9.49 ± 4.79	64.12 ± 31.02
SA Blood	1.12 ± 0.90	7.64 ± 4.99	34.11 ± 18.93
SA Wall	1.93 ± 1.70	11.54 ± 9.08	48.20 ± 28.59
Total	1.51 ± 0.44	8.90 ± 2.07	39.79 ± 18.92
<b>C-P</b>			
LA Blood	1.27 ± 0.71	6.34 ± 2.41	34.39 ± 18.62
LA Wall	2.82 ± 1.14	10.37 ± 1.23	93.90 ± 10.52
SA Blood	1.11 ± 0.69	7.72 ± 4.27	32.57 ± 17.75
SA Wall	3.09 ± 2.62	14.95 ± 10.25	69.71 ± 31.10
Total	2.07 ± 1.03	9.84 ± 3.79	57.64 ± 29.61
<b>E-E</b>			
LA Blood	1.07 ± 0.70	<b>5.26 ± 3.26</b>	19.96 ± 13.34
LA Wall	2.74 ± 1.75	13.52 ± 8.63	69.89 ± 32.08
SA Blood	0.95 ± 0.70	6.36 ± 4.29	28.75 ± 15.87
SA Wall	<b>1.16 ± 0.86</b>	7.76 ± 6.63	40.08 ± 16.43
Total	1.48 ± 0.84	8.22 ± 3.68	39.67 ± 21.77
<b>SPD</b>			
LA Blood	<b>1.06 ± 0.57</b>	5.79 ± 3.41	<b>17.14 ± 8.21</b>
LA Wall	<b>1.52 ± 1.12</b>	<b>8.31 ± 6.17</b>	50.67 ± 33.25
SA Blood	<b>0.73 ± 0.54</b>	<b>5.59 ± 3.90</b>	<b>27.98 ± 16.45</b>
SA Wall	1.19 ± 0.95	7.74 ± 6.88	<b>37.90 ± 17.93</b>
Total	<b>1.13 ± 0.33</b>	<b>6.86 ± 1.37</b>	<b>33.42 ± 14.29</b>

### 3.2. Results for liver CT

Given that C-P behaves like AF, it has been dropped for this experiment. Manual segmentations (available at <http://www.sliver07.org/>) were defined as the entire liver tissue including all internal structures like vessel systems, tumors, etc. Such structures present a different gray-level than healthy liver tissue and might not be included in the k-means segmentation. Morphological operations have been applied to k-means in order to include such structures.

The main difficulty in CT is that contrast sharpness might be at the cost of noise increase. This property splits CT into two main categories. Images with a clear inter-tissue transition but a low signal-to-noise ratio (data sets CT1, CT2) and images with a good signal present but a poor inter-tissue contrast (data sets CT3 to CT5). For the first type, a filter with strong regularizing properties should be used, while for the second type the filter should preserve image sharpness as much as possible in order to avoid merging of different structures.

Fig. 3 shows the performance for two representative CT images, a noisy image from CT1 in Fig. 3(a) and a poor contrast one from CT3 in Fig. 3(c). Like Fig. 2, manual contours are plotted in red on segmented images (Fig. 3(b), (d)) and also on the non-processed ones for a better discrimination of the liver. As in the previous experiment, Table 2 (also split into blocks) reports ranges for the quality scores with merit numbers in boldface. Infinite for distances indicates that liver contours were undetected for some images.

The segmentation of the liver area fails for some images in non-processed volumes (infinite AvSD ranges for CT1, CT2 in the first

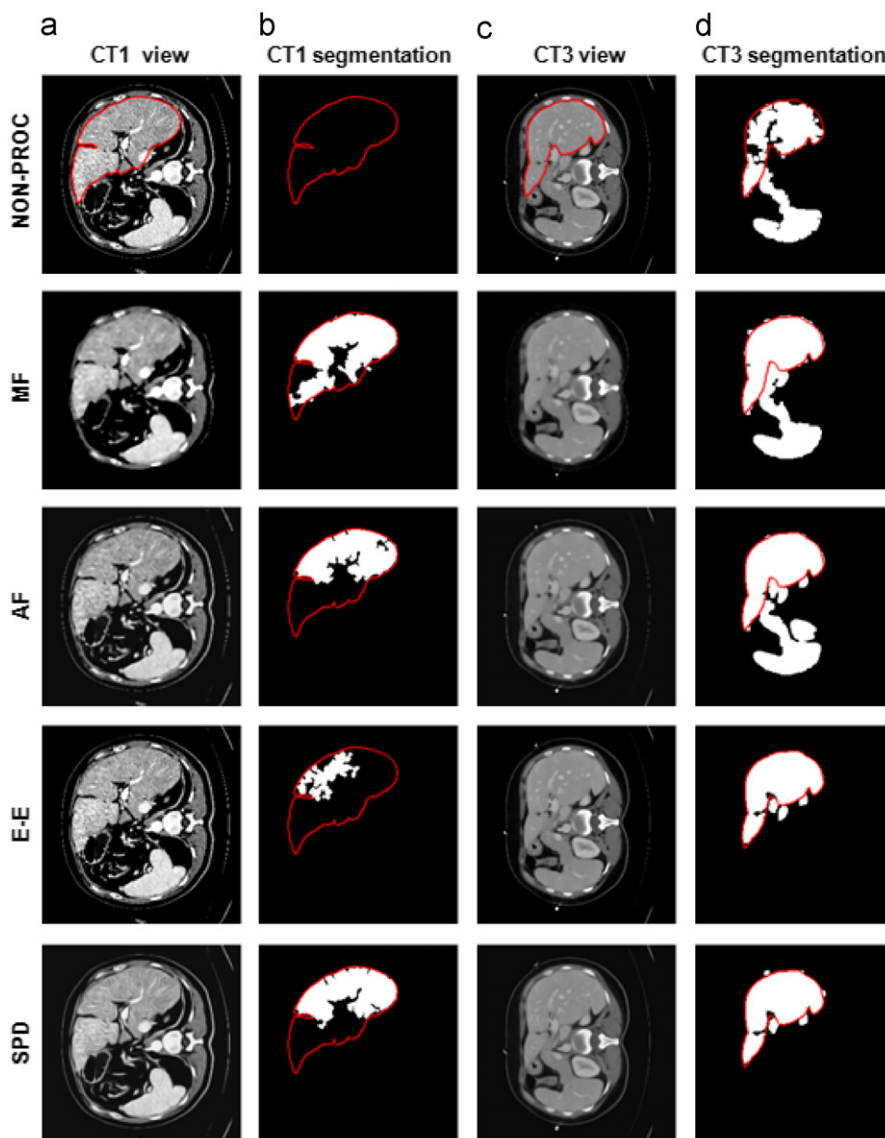


Fig. 3. Performance of smoothing approaches on Liver CT.

block) and is prone to merge the liver with adjacent tissue in low contrast ones (MxSD ranges for CT3–CT5 and Fig. 3(d), 1st row). By its strong smoothing properties, MF outperforms PDE-based methods in noisy volumes (especially for highly noisy cases like CT1 shown in Fig. 3(b)). However, its efficiency might significantly drop in low contrast cases by a systematic merging of adjacent tissue (AvSD ranges for CT3 as shown in Fig. 3(d), 2nd row). Over regularization of AF images also produce tissue merging in low contrast cases (CT3, CT4) as illustrated in Fig. 3(d), 3rd row. Given that low-contrast cases are quite smooth, E-E performance is optimal as illustrated in Fig. 3(d), 4th row. However, for noisy cases it might amplify noise (see Fig. 3(b), 4th row) producing rather erroneous segmentations (like Vol1 in Table 2). Finally, SPD achieves a suitable compromise between noise removal and preservation of intensity sharpness and structures geometry. It follows that it gets the best total ranges for all scores.

#### 4. Application to extraction of plant's xylem network

The xylem of plants is a tissue consisting of a tubular network that provides the main pathway for long distance transport of

water from roots to leaves [25]. Its properties determine how much water can be transported by plants, as well as the vulnerability to transport dysfunctions (formation and propagation of emboli) associated to stress factors, such as droughts and frost. In particular, vulnerability to embolism has been recognized as one of the main factors explaining plants' resistance to drought and a key element in predicting plant survival under warmer (and drier) conditions [26]. A proper description of the structure and transport properties of the xylem is thus a key element in the development of realistic predictive models of the behavior of different plant species under extreme drought conditions and to forecast vegetation changes under different climate change scenarios [27].

The relationship between xylem structure and function has traditionally been studied from 2D cross-sections of the xylem tissue (e.g. [25]), using properties such as the diameter- ( $\sim \mu\text{m}$ ) and length- ( $\sim \text{cm}$ ) distributions of the conduits and the size of the pores that connect them. Recent studies [28], however, show the importance of the 3D topology of the xylem network to its overall transport properties. Specifically, the connectivity of the system (i.e. the average number of neighbors per conduit) has a strong effect on both the hydraulic conductivity of the xylem

**Table 2**  
Quality scores ranges for liver CT-images.

	AvSD	MxSC	VOE
Non-proc			
CT1	$\infty$	$\infty$	99.26 $\pm$ 3.46
CT2	$\infty$	$\infty$	84.96 $\pm$ 24.58
CT3	3.31 $\pm$ 4.02	32.34 $\pm$ 27.21	22.15 $\pm$ 11.29
CT4	<b>1.27 <math>\pm</math> 1.22</b>	<b>14.84 <math>\pm</math> 13.35</b>	<b>9.45 <math>\pm</math> 6.40</b>
CT5	1.45 $\pm$ 1.35	15.07 $\pm$ 11.98	13.71 $\pm$ 11.76
Total	$\infty$	$\infty$	45.91 $\pm$ 42.73
MF			
CT1	<b>3.66 <math>\pm</math> 4.74</b>	<b>31.70 <math>\pm</math> 27.04</b>	<b>26.10 <math>\pm</math> 13.56</b>
CT2	2.44 $\pm$ 4.73	17.18 $\pm$ 25.65	<b>9.29 <math>\pm</math> 11.99</b>
CT3	6.51 $\pm$ 6.00	47.29 $\pm$ 30.89	22.91 $\pm$ 12.64
CT4	3.11 $\pm$ 5.07	22.75 $\pm$ 28.60	11.30 $\pm$ 9.29
CT5	2.99 $\pm$ 4.83	24.24 $\pm$ 27.21	10.61 $\pm$ 7.95
Total	3.74 $\pm$ 1.61	28.63 $\pm$ 11.65	16.04 $\pm$ 7.84
AF			
CT1	5.54 $\pm$ 5.26	49.46 $\pm$ 31.98	33.52 $\pm$ 14.38
CT2	1.79 $\pm$ 2.95	14.71 $\pm$ 19.86	11.35 $\pm$ 13.46
CT3	7.72 $\pm$ 8.41	44.68 $\pm$ 38.81	23.30 $\pm$ 18.91
CT4	7.27 $\pm$ 5.59	46.37 $\pm$ 30.08	29.09 $\pm$ 7.82
CT5	2.15 $\pm$ 2.32	19.81 $\pm$ 18.95	8.89 $\pm$ 6.43
Total	4.90 $\pm$ 2.79	35.01 $\pm$ 16.39	21.23 $\pm$ 10.81
E-E			
CT1	12.67 $\pm$ 10.96	62.82 $\pm$ 32.13	70.66 $\pm$ 20.10
CT2	<b>1.37 <math>\pm</math> 1.05</b>	<b>12.99 <math>\pm</math> 10.40</b>	10.97 $\pm$ 7.52
CT3	1.63 $\pm$ 1.41	16.93 $\pm$ 14.19	10.47 $\pm$ 8.98
CT4	2.33 $\pm$ 3.70	19.08 $\pm$ 21.71	9.57 $\pm$ 6.57
CT5	<b>1.33 <math>\pm</math> 1.26</b>	<b>14.35 <math>\pm</math> 13.66</b>	<b>7.72 <math>\pm</math> 5.36</b>
Total	3.87 $\pm$ 4.94	25.23 $\pm$ 21.14	21.88 $\pm$ 27.30
SPD			
CT1	6.08 $\pm$ 5.67	48.87 $\pm$ 30.86	36.37 $\pm$ 16.34
CT2	1.65 $\pm$ 1.80	14.58 $\pm$ 13.48	12.09 $\pm$ 10.68
CT3	<b>1.60 <math>\pm</math> 1.34</b>	<b>16.74 <math>\pm</math> 14.33</b>	<b>10.24 <math>\pm</math> 8.62</b>
CT4	2.37 $\pm$ 3.43	20.97 $\pm$ 22.60	9.98 $\pm$ 7.06
CT5	1.47 $\pm$ 1.32	17.05 $\pm$ 15.81	8.30 $\pm$ 6.60
Total	<b>2.63 <math>\pm</math> 1.96</b>	<b>23.64 <math>\pm</math> 14.29</b>	<b>15.40 <math>\pm</math> 11.80</b>

and its vulnerability to embolism [28]. Unfortunately, measuring the connectivity of real wood samples remains a challenge, as obtaining good quality 3D reconstructions of representative segments of the xylem network is technically difficult because of the required spatial resolution and the opacity of wood.

X-ray computed micro-tomography (micro-CT) is one of the few imaging techniques allowing high resolution imaging of the 3D xylem network [29,30]. In order to process stacks of micro-CT sections to obtain good quality 3D reconstructions of the xylem network that are useful to estimate its connectivity, it is critical that the segmentation algorithm preserves all the functional conduits (i.e. even the smallest ones) and that neighbor conduits are not merged. Fig. 4 shows how SPD smoothing can be used in this context to produce satisfactory results. Fig. 4(a) shows a tomographic section of a wooden segment from *Fraxinus americana*, obtained with a SkyScan 1072 microtomograph [30], and its processed SPD output is shown in Fig. 4(b). Xylem conduits correspond to darker elliptic structures and might appear either isolated or in small (connected) groups separated by a (lighter) thin cell wall. Fig. 4(d) and (e) show gray-level intensity histograms for non-processed (Fig. 4(d)) and SPD (Fig. 4(e)) images. In the SPD processed image, even the smallest conduits (like the one in square 1) are clearly outlined from the background and there is no loss (i.e. conduit merging) in their connectivity (see the two neighbors in square 2). Furthermore, SPD homogenization of structure intensity produces a bi-modal distribution in histograms clearly separating xylem tubes from background. We have used this property to obtain a detailed 3D reconstruction of the xylem system by simple image processing operators.

Otsu's thresholding method applied to each CT-slice histogram gives the gray-value (vertical dashed line in histogram of Fig. 4(e)) that best separates the two distributions. Morphological operations on binary images are used to remove small structures and close tube holes. Fig. 4(c) shows the final binary image representing xylem tubes from SPD image in Fig. 4(b). A labeling of the binary 3D block provides the xylem network (as shown in Fig. 4(f)) and allows the computation of the network connectivity by morphological opening with a structure element of size the maximum separation between connected tubes. These results provide one of the first direct measurements of the connectivity of the xylem network in any plant species, and are consistent with previous manual measurement attempts (cf. [31] for *Fraxinus excelsior*). Additionally, SPD smoothing has been recently applied to improve the segmentation of traditional xylem cross-sections (2D) in a work looking at the spatial distribution of xylem conduits and its functional significance [32].

## 5. Conclusions

Smoothing of biomedical images preserving weak tissue transitions is a crucial step for a proper segmentation of anatomical structures. Smoothing methods given by solutions to a second order elliptic PDE are backed up by a solid mathematical theory and admit an explicit iterative numeric scheme. The asymptotic behavior of solutions is determined by the second order term, which is usually described by means of a diffusion tensor positive defined. If the eigenvectors of strictly positive eigenvalues expand the whole space, solutions converge towards a constant function and the number iterations becomes a critical issue.

This work gives the mathematical conditions required for designing tensors that do not expand the whole space, but restrict diffusion to given manifolds. The condition is always satisfied for eigenvectors perpendicular to a single smooth vector field, which, in the case of images, might be computed using the structure tensor. The diffusion scheme is the implicit formulation of an elliptic operator on the integral manifolds of the eigenvectors of strictly positive eigenvalues. By using the structure tensor for defining such eigenvectors, they model a smooth completion of anatomical structures and expand the whole space elsewhere. It follows that the diffusion scheme converges to non-uniform images which present homogenous inter-tissue transitions at consistent anatomical structures and are smooth everywhere else. By using an implicit formulation, our restricted diffusion admits an explicit numeric scheme for non-linear heat equations which stops by stabilization of the iterative scheme.

Thus, the proposed diffusion has several advantages over existing second order PDE-based methods. It can be solved using a low complexity numeric scheme supported for any dimension and which only depends on the two parameters used to compute the structure tensor. The stopping criterion for the iterative numeric scheme is independent of the input image. The stabilized solutions preserve intensity sharpness and the geometry of structures in a natural way. By its geometric nature, SPD preserves low contrast structures as far as their geometry is well defined. This is an advantage over other PDE techniques using structure tensor since they would smooth them out if they have a well-defined geometry but low contrast. Another main advantage is the ability to restore thin structures and homogenize the response to local image descriptors.

The performance of SPD strongly relies on the quality of vector fields representing the tangent space of anatomical structures. In this approach, the structure tensor has been used, which makes the proposed diffusion fail in three specific situations. First, like other methods based on the structure tensor, diffusion is not well

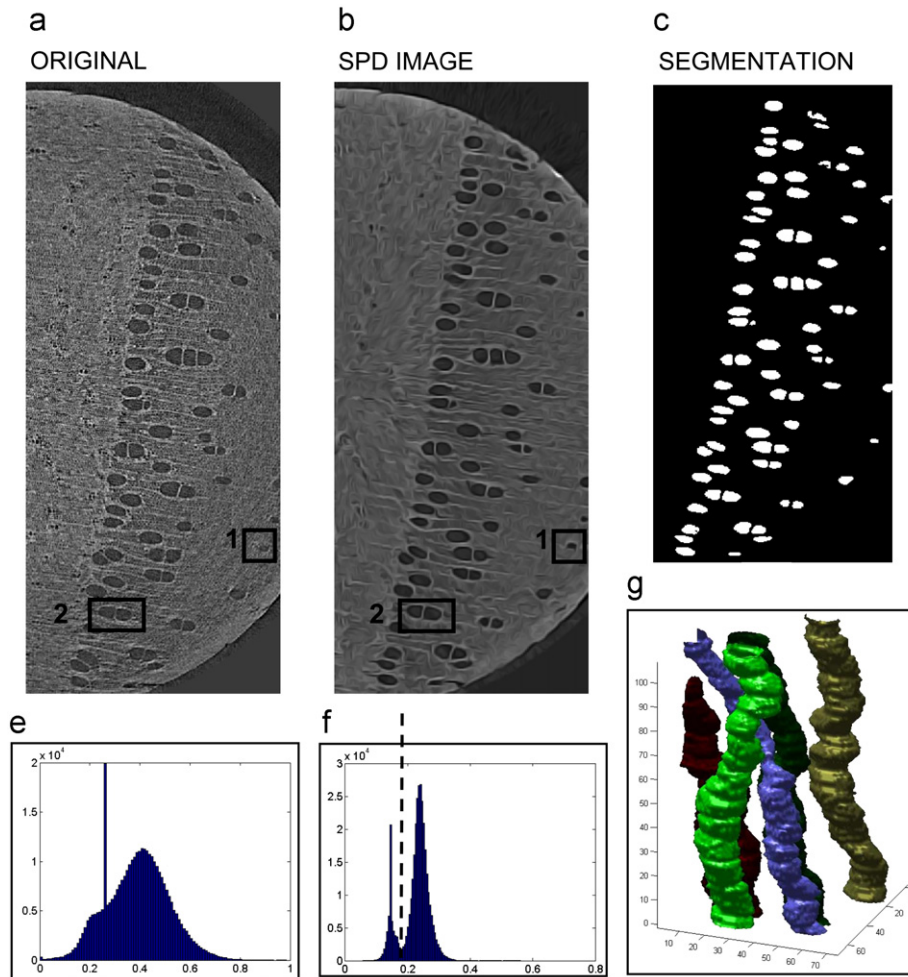


**Fig. 4.** Benefits of SPD on micro-CT slices of wooden segment. Top images show non-processed (a), SPD (b), and segmented CT-slices (c). Bottom graphics show intensity histograms for non-processed (d), SPD images (e), and 3D-reconstruction of the xylem (f).

defined at corners, where level-curves tangent space is not consistent. Since this represents a significant limitation in natural scenes, there are some recent methods trying to fix the problem [33]. Fortunately, biomedical structures have smooth boundaries, so that, in the particular field of biomedical imaging filtering SPD is reliable. Second, we have observed that at areas presenting heavy speckle noise, the structure tensor might produce fake consistent vector fields partially aligned along observable noisy patterns. In such situations, SPD is prone to introduce false boundaries inside anatomic structures. This might be solved by tuning of the structure tensor scales or using alternative measures of image local structure. Finally, by its geometric nature, SPD might smooth out small structures (such as tumors and polyps) in the case that the structure tensor cannot model their tangent space. The number of smooth out small structures is minimized by considering the smallest scales for computing the structure tensor. We consider that structures below such scales are on the edge of the image resolution and thus their measurement is not accurate enough for medical applications.

#### Acknowledgments

We would like to thank Francesc Carreras and Xavier Alomar from the Radiology Department of Creu Blanca clinic for providing MR data. This work was supported by the Spanish projects PI071188, TIN2009-13618, CSD2007-00018 and Explora (CGL2007-28784-E). The first author has been supported by The Ramon y Cajal Program.

#### Appendix A. Relation to the heat equation on manifolds

As in the case of  $\mathbb{R}^n$ , heat equations on manifolds,  $M$ , are given by divergence operators  $\text{div}_M(J\nabla I)$ , for  $J$  a symmetric positive defined 2-form (i.e. a metric),  $\nabla I$  the gradient (in  $M$ ) of a smooth function,  $I : M \rightarrow \mathbb{R}$ , and the divergence operator defined on  $M$ . In order to deduce the expression in  $M$  coordinates and its relation to our structure-preserving smoothing, we will use some tools of differential geometry. General theory on Riemannian manifolds might be found in [20] and the specific one about heat equations on manifolds in [21].

We will use the following notations. Scalar product will be noted by  $\langle \cdot, \cdot \rangle$ , the divergence of a vector field by  $\text{div}$ , Lie derivatives by  $L$  and the Lie bracket by  $[\cdot, \cdot]$ . Given a  $k$ -dimensional Riemannian manifold,  $M$ , we will use the subindex  $M$  to indicate that the former operators are taken on  $M$ . In the particular case of  $\mathbb{R}^n$  the subindexes will be dropped. Coordinates will be noted by  $s = (s_1, \dots, s_k)$  for  $M$  and by  $x = (x_1, \dots, x_n)$  for  $\mathbb{R}^n$ . Accordingly, basis of the respective tangent (vector) spaces will be given by the partial derivatives  $\partial_{s_i}$ ,  $i = 1, \dots, k$  and  $\partial_{x_i}$ ,  $i = 1, \dots, n$ .

The expression of any vector field,  $\tilde{\xi}$ , in local coordinates is given by  $\tilde{\xi} = \sum_i \tilde{\xi}_i(s) \partial_{s_i}$ , and will be noted by  $(\tilde{\xi}_1, \dots, \tilde{\xi}_k)$  for short.

If  $M$  is embedded in  $\mathbb{R}^n$  through local charts  $\phi$ :

$$\phi : U \subset \mathbb{R}^k \rightarrow M \subset \mathbb{R}^n$$

$$s = (s_1, \dots, s_k) \mapsto (\phi_1(s), \dots, \phi^n(s))$$

then the Jacobian of the chart:

$$D\phi = \begin{pmatrix} \partial_{s_1} \phi_1 & \cdots & \partial_{s_k} \phi_1 \\ \vdots & & \vdots \\ \partial_{s_1} \phi_n & \cdots & \partial_{s_k} \phi_n \end{pmatrix} \quad (4)$$

is a  $k \times n$  matrix that provides an expression of the vectors  $\partial_{s_i}$  in the canonic (vectorial) basis of  $\mathbb{R}^n$ :

$$\partial_{s_i}(\phi) = (\phi_{s_1}^1, \dots, \phi_{s_i}^n) = \phi_{s_1}^1 \partial_{x_1} + \cdots + \phi_{s_i}^n \partial_{x_n} \quad (5)$$

It follows that any vector field on  $M$ ,  $\tilde{\xi} = (\tilde{\xi}_1(s), \dots, \tilde{\xi}_k(s))$ , has an expression in  $\mathbb{R}^n$  given by applying  $D\phi$  to  $\tilde{\xi}$ :

$$\tilde{\xi} = D\phi \tilde{\xi} \quad (6)$$

That is,  $\xi = (\xi_1(X), \dots, \xi_n(X))$ , for  $\xi_k = \sum_i \tilde{\xi}_i \phi_{s_i}^k$ . Conversely, any vector field,  $\xi$ , in  $\mathbb{R}^n$  has an expression in  $M$  given by

$$\tilde{\xi} = (D\phi^t D\phi)^{-1} D\phi^t \xi \quad (7)$$

for  $\xi = (\xi_1(\phi(s)), \dots, \xi_n(\phi(s)))$  evaluated at  $\phi(s)$ .

Manifolds embedded in  $\mathbb{R}^n$  inherit its scalar product, so that  $\langle \cdot, \cdot \rangle_M$  is given by the symmetric tensor  $(g_{ij})_{ij} = (\langle \partial_{s_i}, \partial_{s_j} \rangle)_{ij}$  for  $\partial_{s_k}$  given by (5). If  $g = \det(g_{ij})$  denotes its determinant, then the volume form of  $M$  equals  $\omega = g^{1/2} ds_1 \dots ds_k$ , for  $ds_i$  the dual basis of  $\partial_{s_i}$ .

The divergence of a vector field  $\tilde{\xi}$  in local coordinates is [20]

$$\operatorname{div}_M(\tilde{\xi}) = g^{-1/2} \tilde{\xi} (g^{1/2}) + \sum_i \partial_{s_i}(\tilde{\xi}^i) \quad (8)$$

Given a smooth function  $I = I(s_1, \dots, s_k) : M \rightarrow \mathbb{R}$ , its gradient in  $M$  is the (unique) vector satisfying [21]

$$\langle \nabla_M I, \tilde{\xi} \rangle_M = \sum_k \tilde{\xi}^k \partial_{s_k} I = \tilde{\xi}(I) = I_{\tilde{\xi}} \quad (9)$$

Analogously to  $\mathbb{R}^n$ ,  $\nabla I$  might be interpreted as the vector that provides the derivative of the function along any direction  $\tilde{\xi}$ . In the case that  $I = I(x_1, \dots, x_n)$  is a function of  $\mathbb{R}^n$  restricted to  $M$ , we have that the derivative in  $\mathbb{R}^n$  relates to the derivative in  $M$ :

$$\begin{aligned} \langle \nabla I, \xi \rangle &= \sum_k \xi^k \partial_{x_k} I = \sum_k \partial_{x_k} I \left( \sum_i \tilde{\xi}_i \phi_{s_i}^k \right) \\ &= \sum_i \tilde{\xi}_i \left( \sum_k \phi_{s_i}^k \partial_{x_k} I \right) = \sum_i \tilde{\xi}_i \partial_{s_i} I = \langle \nabla_M I, \tilde{\xi} \rangle_M \end{aligned} \quad (10)$$

Expression (5)–(10) is all we need to compute the formulation of the heat equation on manifolds and relate it to our restricted diffusion. Let  $\tilde{\xi}_1, \dots, \tilde{\xi}_k$  be the eigenvectors of a diffusion tensor with  $\lambda^i = 1$  defined on a manifold  $M$ . The associated heat equation is given by [21]

$$\begin{aligned} \operatorname{div}_M(J\nabla_M u) &= \operatorname{div}_M \left( \sum_i \langle \nabla_M u, \tilde{\xi}^i \rangle_M \cdot \tilde{\xi}^i \right) \\ &= \sum_i \langle \nabla_M u, \tilde{\xi}^i \rangle_M \cdot \operatorname{div}_M(\tilde{\xi}^i) + \sum_i \tilde{\xi}^i (\langle \nabla_M u, \tilde{\xi}^i \rangle_M) \\ &= \sum_i u_{\tilde{\xi}^i} \operatorname{div}_M(\tilde{\xi}^i) + \sum_i u_{\tilde{\xi}^i \tilde{\xi}^i} + \sum_i \langle \nabla_M u, (\nabla_M \tilde{\xi}^i) \tilde{\xi}^i \rangle_M \end{aligned} \quad (11)$$

where  $\nabla_M \tilde{\xi}^i$  stands for the Jacobian of a vector  $\tilde{\xi}^i = (\tilde{\xi}_1^i, \dots, \tilde{\xi}_k^i)$  in local coordinates:

$$\nabla_M \tilde{\xi}^i = \begin{pmatrix} \partial_{s_1} \tilde{\xi}_1^i & \cdots & \partial_{s_k} \tilde{\xi}_1^i \\ \vdots & & \vdots \\ \partial_{s_1} \tilde{\xi}_k^i & \cdots & \partial_{s_k} \tilde{\xi}_k^i \end{pmatrix}$$

and  $u_{\tilde{\xi}^i \tilde{\xi}^i}$  is the second derivative along  $\tilde{\xi}^i$  given by the Hessian in  $M$ :

$$(u_{\tilde{\xi}^i \tilde{\xi}^i})_{ij} = (\tilde{\xi}_j^i)^t (u_{s_i s_j})_{ij} (\tilde{\xi}_j^i)_{ij}$$

The Laplacian corresponds to  $\tilde{\xi}^i = \partial_{s_i}$ .

Since the second order term in (11) is of elliptic type, there is a unique solution [19]. In fact, since  $\tilde{\xi}^i$  are orthonormal, the matrix  $(u_{\tilde{\xi}^i \tilde{\xi}^i})_{ij}$  is equivalent (as linear map) to  $(u_{s_i s_j})_{ij}$ . Therefore, by invariance of traces under coordinate changes, we have that (11) equals

$$\underbrace{\sum_i u_{s_i s_i}}_{\text{2nd order}} + \underbrace{\sum_i \operatorname{div}_M(\tilde{\xi}^i) u_{\tilde{\xi}^i} + \langle \nabla_M u, (\nabla_M \tilde{\xi}^i) \tilde{\xi}^i \rangle_M}_{\text{1st order}} \quad (12)$$

We would like to note that by (8) diffusion equations on manifolds contain, in the general case, a divergence term of the eigenvectors of the diffusion tensor. However, this term does not influence the asymptotic behavior of solutions, since it is exclusively determined by the second order term.

In the case of the restricted diffusion introduced in Section 2, the divergence develops as

$$\operatorname{div}(J\nabla u) = \sum_i u_{\xi^i} \operatorname{div}(\xi^i) + \sum_i u_{\xi^i \xi^i} + \sum_i \langle \nabla u, (\nabla \xi^i) \xi^i \rangle \quad (13)$$

for derivatives taken in  $\mathbb{R}^n$ . By using the expression of  $\xi^i$  in  $M$  coordinates given by (7), we have that

$$(u_{\xi^i \xi^j})_{ij} = (\xi_j^i)^t (u_{x_i x_j})_{ij} (\xi_j^i)_{ij} = \left( \begin{array}{c|c} (\tilde{\xi}_j^i)^t (u_{s_i s_j})_{ij} (\tilde{\xi}_j^i)_{ij} & 0 \\ \hline 0 & 0 \end{array} \right)$$

This relation and (10) imply that (13) is equal to

$$\operatorname{div}_{\mathbb{R}^n}(J\nabla u) = \sum_i u_{s_i s_i} + \sum_i u_{\tilde{\xi}^i} \operatorname{div}(\tilde{\xi}^i) + \sum_i \langle \nabla_M u, (\nabla_M \tilde{\xi}^i) \tilde{\xi}^i \rangle_M \quad (14)$$

The main difference between (14) and (12) is the divergence of the vector fields, which is computed on each space ( $M$  for (12) and  $\mathbb{R}^n$  for (14)). This difference does not affect steady states, which are described by functions constant on the integral manifolds of the distribution  $(\xi^1, \dots, \xi^k)$ .

## References

- [1] W. Pratt, Digital Image Processing, Wiley, 1998.
- [2] D. Comaniciu, P. Meer, Mean shift analysis and applications, in: International Conference on Computer Vision (ICCV), 1999.
- [3] G. Papari, N. Petkov, P. Campisi, Artistic edge and corner enhancing smoothing, IEEE Trans. Imag. Process. 16 (10) (2007) 2449–2462.
- [4] S. Osher, A. Sole, L. Vese, Image decomposition and restoration using total variation minimization and the  $h_1$  norm, Multiscale Model. Simul. 1 (2003) 349–370.
- [5] L. Evans, Partial Differential Equations, Berkeley Mathematics Lecture Notes, 1993.
- [6] P. Perona, J. Malik, Scale space and edge detection using anisotropic diffusion, IEEE Trans. Pattern Anal. Mach. Intell. 12 (7) (1990) 629–639.
- [7] P. Saha, J. Udupa, D. Odhner, Scale-based fuzzy connected image segmentation: theory, algorithms and validation, Comput. Vis. Imag. Unders. 77 (2000) 145–174.
- [8] H. Salinas, D. Fernandez, Comparison of PDE-based nonlinear diffusion approaches for image enhancement and denoising in optical coherence tomography, IEEE Trans. Med. Imag. 26 (6) (2007) 761–771.
- [9] P.K. Saha, J. Udupa, Scale-based diffusive image filtering preserving boundary sharpness and fine structures, IEEE Trans. Med. Imag. 20 (2001) 1140–1155.
- [10] J. Weickert, A review of nonlinear diffusion filtering, in: Scale-space Theory in Computer Vision, Springer-Verlag 1997, pp. 3–28.
- [11] R. Manniesing, M. Viergever, W. Niessen, Vessel enhancing diffusion a scale space representation of vessel structures, Med. Imag. Anal. 10 (2006) 815–825.
- [12] K. Chen, Adaptive smoothing via contextual and local discontinuities, IEEE Trans. Pattern Anal. Mach. Intell. 27 (10) (2005) 1552–1567.
- [13] P. Charbonnier, L. Blanc-Feraud, G.A.M. Barlaud, Deterministic edge-preserving regularization in computed imaging, IEEE Trans. Imag. Process. 6 (2) (1997) 298–311.

- [14] L. Rudin, S. Osher, E. Fatemi, Nonlinear total variation based noise removal algorithms, *Phys. D* 60 (1992) 259–268.
- [15] E. Tadmor, S. Nezzar, L. Vese, A multiscale image representation using hierarchical (BV, L2) decomposition, *Multiscale Model. Simul.* 2 (2004) 554–579.
- [16] D. Tschumperle, Fast anisotropic smoothing of multi-valued images using curvature-preserving pde's, *Int. J. Comput. Vis.* 68 (1) (2006) 65–82.
- [17] B. Cabral, L. Leedom, Imaging vector fields using line integral convolution, in: *SIGGRAPH 1993, Computer Graphics*, 1993, pp. 263–272.
- [18] W. Press, B. Flannery, S. Teukolsky, W. Vetterling, *Numerical Recipes in C*, Cambridge University Press, 1997.
- [19] D. Gil, Geometric differential operators for shape modelling, Ph.D. Thesis, Universitat Autònoma de Barcelona, 2004.
- [20] M. Spivak, *A Comprehensive Introduction to Differential Geometry*, vol. 1, Publish or Perish, Inc., 1999.
- [21] E. Davies, *Heat Kernels and Spectral Theory*, Cambridge University Press, 1989.
- [22] T. Heimann, B. van Ginneken, M. Styner, Y. Arzhaeva, V. Aurich, et al., Comparison and evaluation of methods for liver segmentation from ct datasets, *IEEE Trans. Med. Imag.* 28 (8) (2009) 1251–1265.
- [23] R. Cardenas, M. Bach, Y. Chi, et al., Multimodal evaluation for medical image segmentation, in: *International Conference on Analysis of Image Processing (CAIP)*, 2007.
- [24] D. Gil, P. Radeva, A regularized curvature flow designed for a selective shape restoration, *IEEE Imag. Process.* 13 (11) (2004) 1444–1458.
- [25] M. Tyree, M. Zimmermann, *Xylem Structure and the Ascent of Sap*, Springer-Verlag, 2002.
- [26] N. McDowell, W. Pockman, C. Allen, D. Breshears, N. Cobb, T. Kolb, J. Plaut, J. Sperry, A. West, D. Williams, E. Yepez, Mechanisms of plant survival and mortality during drought: Why do some plants survive while others succumb to drought? *New Phytol.* 178 (2008) 719–739.
- [27] P. Ciais, M. Reichstein, N. Viovy, et al., Europe-wide reduction in primary productivity caused by the heat and drought in 2003, *Nature* 437 (2005) 529–533.
- [28] L. Loeffe, J. Martinez-Vilalta, J. Piñol, et al., The relevance of xylem network structure for plant hydraulic efficiency and safety, *J. Theor. Biol.* 247 (2007) 788–803.
- [29] P. Trtik, J. Dual, D. Keunecke, et al., 3d imaging of microstructure of spruce wood, *J. Struct. Biol.* 159 (2007) 45–56.
- [30] K. Steppe, V. Cnudde, C. Girard, R. Lemeur, J.-P. Cnudde, P. Jacobs, Use of X-ray computed microtomography for non-invasive determination of wood anatomical characteristics, *J. Struct. Biol.* 148 (2004) 11–21.
- [31] P. Burggraaf, Some observations on the course of the vessels in the wood of *Fraxinus excelsior*, L., *Acat Bot. Neerl.* 21 (1972) 32–47.
- [32] M. Mencuccini, J. Martinez-Vilalta, J. Piñol, L. Loeffe, M. Burnat, X. Alvarez, J. Camacho, D. Gil, A statistical approach to the determination of xylem conduit spatial distribution, *Am. J. Bot.* 97 (8) (2010) 1247–1259.
- [33] E. Franken, R. Duits, Crossing-preserving coherence-enhancing diffusion on invertible orientation scores, *Int. J. Comput. Vis.* 85 (2009) 253–278.

**Debora Gil** received her degree in Mathematics from Universitat de Barcelona in 1994 and her PhD from Universitat Autònoma de Barcelona (UAB, Bellaterra, Spain) in 2004. Since 1997 she has been working for the Computer Vision Center (CVC) and the Computer Science Department of Universitat Autònoma de Barcelona. She is in charge of the Modelling and Visualization group in CVC since 2007. Her main interests are mathematical tools applied to image processing (especially, but not exclusively, biomedical imaging) and she has expertise in pde-based methods, segmentation, motion analysis and shape modelling.

**Aura Hernandez** received her degree in Mathematics from Universitat Autònoma de Barcelona (UAB, Bellaterra, Spain) in 2002. In 2005 and 2009, respectively, she received her MSc and PhD in Computer Science from the UAB. She is a lecturer at UAB and collaborates with the Computer Vision Center ([www.cvc.uab.es](http://www.cvc.uab.es)). Her research interests are focused on Image Processing Techniques for Biomedical Images, such as, segmentation, and dynamical parameters estimation, and mathematical models for Biomedical Image Processing, like contour geometry, geometric flows and variational models.